Acta Materialia 217 (2021) 117122

Contents lists available at ScienceDirect

Acta Materialia

journal homepage: www.elsevier.com/locate/actamat

Full length article

Understanding imprint formation, plastic instabilities and hardness evolutions in FCC, BCC and HCP metal surfaces

Javier Varillas[a,b], Jan Očenášek[a], Jordi Torner[c], Jorge Alcalá[c,*]

[a] New Technologies Research Centre, University of West Bohemia in Pilsen, 30614 Plzeň, Czech Republic
[b] Institute of Thermomechanics, Czech Academy of Sciences, 182 00 Prague 8, Czech Republic.
[c] InSup, ETSEIB and b_TEC, Universitat Politècnica de Catalunya, 08028 Barcelona, Spain

ARTICLE INFO

Article history:
Received 25 February 2021
Revised 16 June 2021
Accepted 17 June 2021
Available online 7 July 2021

Keywords:
Nanoindentation
Hardness
Dislocations
Twinning
Crystal plasticity

ABSTRACT

Nanoindentation experiments in metal surfaces are characterized by the onset of plastic instabilities along with the development of permanent nanoimprints and dense defect networks. This investigation concerns massive molecular dynamics simulations of nanoindentation experiments in FCC, BCC and HCP metals using blunted (spherical) tips of realistic size, and the detailed comparison of the results with experimental measurements. Our findings shed light on the defect processes which dictate the contact resistance to plastic deformation, the development of a transitional stage with abrupt plastic instabilities, and the evolution towards a self-similar steady-state characterized by the plateauing hardness p_p at constant dislocation density ρ_p. The onset of permanent nanoimprints is governed by stacking fault and nanotwin interlocking, the buildup of nanostructured regions and crystallites throughout the imprint, the cross-slip and cross-kinking of surfaced screw dislocations, and the occurrence of defect remobilization events within the plastic zone. As a result of these mechanisms, the ratio between the hardness p_p and the Young's modulus E becomes higher in BCC Ta and Fe, followed by FCC Al, HCP Mg and large stacking fault width FCC Ni and Cu. Finally, when nanoimprint formation is correlated with the uniaxial response of the indented minuscule material volume, the hardness to yield strength ratio, p_p/σ_{ys}, varies from $\approx$7 to $\approx$10, which largely exceeds the continuum plasticity bound of $\approx$2.8. Our results have general implications to the understanding of indentation size-effects, where the onset of extreme nanoscale hardness values is associated with the occurrence of unique imprint-forming processes under large strain gradients.

1. Introduction

The plastic response of metal surfaces at the nanoscale can be effectively probed through nanoindentation experiments. Numerous investigations in this field concern the onset of the first plastic instability or pop-in event, produced during the incipient penetration of a blunt nanoindenter tip *via* prismatic dislocation loop or specific nanotwin emission processes in ideally, atomistically flat surfaces (e.g., see [1–5]); defect nucleation in stepped or curved surfaces (e.g., see [6,7]); and mobilization of preexisting dislocations in plastically strained materials (e.g., see [8–11]). As the nanoindenter tip penetrates onto the surface, the development of secondary plastic instabilities or strain bursts has been extensively reported. While the size of the strain bursts varies with crystal structure, applied load, surface orientation and temperature (e.g., see [4,12–15]), a fundamental understanding is still unavailable on the underlying collective defect processes.

Continuum crystal plasticity analyses of indentation experiments have been successfully used to test our knowledge of dislocation glide and twinning under complex three-dimensional stress fields (e.g., see [16–20]). In these investigations, permanent imprint formation and the resulting material hardness become a fingerprint of the specific defect processes by which the material deforms at the plastic zone beneath the surface, thus providing a self-consistent foundation to the assessment of plastic yielding through indentation testing. While these results concern micrometer-sized indentations, little is known on the defect mechanisms by which permanent imprints develop *at the nanoscale*, or the connection between imprint formation and the defect remobilization phenomena by which plasticity occurs within the nanoindentation plastic zone. An insight into these features is necessary to elucidate the correspondence between nanocontact plasticity —as evaluated through hardness measurements, inden-

* Corresponding author.

https://doi.org/10.1016/j.actamat.2021.117122

tation load–penetration depth curves, and the evolution of the pileup/sink-in responses at the contact rim– and the uniaxial stress–strain curve of the material at the minuscule length scales under consideration, where continuum plasticity potentially breaks down.

This work was initiated to systematically investigate nanocontact plasticity in face-centered cubic (FCC), body-centered cubic (BCC), and hexagonal closed-packed (HCP) metals from the onset of plasticity to the inception of permanent nanoimprints. Our investigation provides an assessment to (i) the intrinsic nanocontact resistance of metal surfaces to defect nucleation and remobilization across a wide range of temperatures and surface orientations, (ii) the evolution of the contact response throughout a transitional regime characterized by large plastic instabilities, and (iii) the instatement of a steady-state regime of smaller instabilities where a plateauing hardness is finally reached. Along these lines, our work represents a systematic attempt to investigate the imprint formation mechanisms that occur in low-load nanoindentation experiments, and to correlate the extreme values of the nanoscale hardness with the onset of plastic yielding within the nanoindentation plastic zone.

2. Methods

This work comprises ≈ 50 large-scale molecular dynamics (MD) spherical indentation simulations performed with the LAMMPS code [21] using embedded-atom method EAM atomic potentials. The potential by Mishin et al. was used to model FCC Al, Cu and Ni [22]; BCC Ta was modelled with the potentials by Li et al. and Ravelo et al. [23,24]; and BCC Fe and HCP Mg were modelled with the potentials by Mendelev et al. and by Sun et al. [25,26], respectively. These computationally efficient EAM potentials developed for metallic material systems have been tested in previous nanoindentation studies [5,27–29], and have been extensively used to investigate metal plasticity in FCC and BCC crystals (see Supplementary Material, S1).

The indentation simulations were performed under the canonical NVT ensemble using the Nosé-Hoover thermostat with timestep of 2 to 3 fs. The penetration of the spherical indenter was modeled through a repulsive potential where the force applied to each atom in contact is prescribed through $F = -K(\frac{D}{2} - \delta)^2;\ \delta \leq D/2$. In this relation, K is the indenter stiffness, D is the indenter diameter, and δ is the distance from the atom to the center of the spherical tip (Supplementary Material, S1). Indenter tips of $D = 24$, 36, 48 and 100 nm were assumed in the simulations, where the greater tip diameter approaches the equivalent sizes of the blunted tips used in nanoindentation experiments. The stiffness K was set to 100 eV/Å^3, which reproduces the applied load–penetration depth ($P - h_s$) curves from coarse-grained elastically anisotropic finite element analyses performed with the stiffness matrices c_{ij} of Al and Ta [15] (Supplementary Material, S1). The indenter velocity, v, was fixed at 4 m/s and 0.2 m/s, which both lie well below the speed of sound and the dislocation glide velocity.

Cuboidal-shaped MD cells of $\approx 70 \times 70 \times 40$ nm^3 that contained ≈ 11 to 16 million atoms depending on lattice parameter and crystal structure were used in the simulations. In the cubic metals, the indented surfaces were of the {100}, {110} and {111} types while in HCP Mg the indented surfaces had the (0001) basal, $(10\bar{1}0)$ prismatic, and $(11\bar{2}2)$ second-order pyramidal orientations. Periodic boundaries were applied to the lateral sides of the MD cells while the atomic positions at the bottom remain fixed in all directions [30] [Following Supplementary Material, S1, note that the influence of the applied boundary conditions on the material hardness can be essentially neglected when the current large MD cells are employed.] The cells were built at 0.1 K and brought to the indentation temperatures of 77 K, 300 K, 400 K, and 900 K at 1 K/ps with timestep of 1 fs. A 100-ps simulation run at vanishing pressure was then applied. Defect visualization was performed through OVITO [31].

The shape of the projected contact area A was approximated using Delaunay triangulation (Supplementary Material, Section S2). This effectively accounts for local irregularities at the contact rim. The associated contact radius was then obtained as $a = \sqrt{A/\pi}$ while the mean contact pressure, or hardness, was computed as $p = P/A$. Imprint formation was further assessed through the pileup parameter $c^2 \equiv h_c/h_s$, where h_s is the total tip penetration and h_c sets the location of the contact radius a along the vertical z-axis (see Fig. 7(d), Section S2 in Supplementary Material and [29]).

Further MD simulations were performed to investigate the remobilization of the defect networks at the indentation plastic zones when subjected to uniaxial loads or to a subsequent indentation loading stage (Supplementary Material, S5). In these simulations, 'prestrained' computational cells were prepared by removing the surface layer that contains the steady-state nanoimprints (Section 3.3). Periodic boundary conditions were then applied, followed by energy minimization and a 50-ps thermalization. The stress–strain curves were recorded by subjecting these MD cells to a uniaxial displacement at a velocity of 0.8m/s ($\dot{\varepsilon} = 1.2 \times 10^7\ s^{-1}$). Alternatively, the subsequent indentation loading was applied with a tip of $D = 48$ nm. [Note that the correlation in Section 3.4 concerned simulations at similar temperatures and comparable loading velocities; Supplementary Material, S5.]

Finally, the dislocation density, ρ, was computed using the total length of the dislocation segments enclosed within the indentation plastic zone, $\rho = l_T/V_{pl}$, where the algorithm in [32] was used to calculate l_T. We assume that the plastic zone has cuboidal shape, $V_{pl} = \kappa a^3$ with $\kappa \approx 28$, in accord with Refs. [33,34] (see Supplementary Material, S6). These ρ measurements include the geometrically necessary dislocations (GNDs), which can be accessed through the crystal rotations (see, e.g., [33,35]). While the evaluation of the hardness p using the GND density has attracted much attention (e.g., [36]), we currently seek to investigate the specific imprint-forming mechanisms in small nanoindentations which are known to contravene such models [37], where twining also plays an important role (Section 3.3).

3. Results and Discussion

3.1. Elastic nanocontacts

Fig. 1(a)-(c) show the applied load to Young's modulus ratio (P/E) vs. penetration depth (h_s) curves from a number of MD simulations. The effective Young's modulus, E, which describes the contact response prior to defect inception is here obtained by fitting applied load and penetration depth data pairs to the linear elastic, Hertzian contact mechanics relation (Ref. [38], Eq. (4.23))

$$P/E = \frac{2\sqrt{2}}{3\left(1-\nu^2\right)} D^{1/2} h_s^{3/2}, \tag{1}$$

where the Poisson ratio, ν, is assumed to remain fixed at 0.3. Wide fluctuations in E are observed within the early indentation stage where contact is established over a minuscule area. The $P - h_s$ curves are then influenced by the spatial arrangement of the surface atoms together with the thermally induced atomic vibrations. These fluctuations vanish with increasing tip penetration, so that when the ratio between the contact radius and the indenter diameter, a/D, surpasses ≈ 0.05 (where $h_s \geq 5$ Å for $D = 42$ nm, with 100 to 300 atoms in contact) the inferred E varies in less than 5%.

As the tip penetration is increased within elasticity, a sustained raise in the effective E results (Figs. 1(e) and (f)) which reaches a maximum of ≈ 25% with respect to the extrapolated E value at

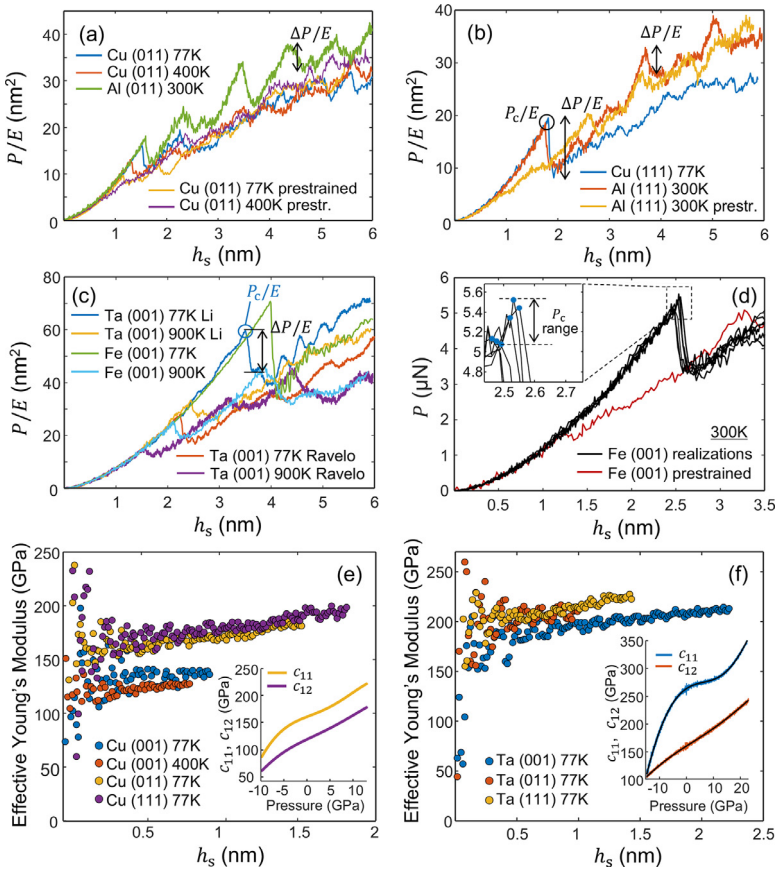

Fig. 1. (a)–(c) Evolutions of the applied load P and the effective Young's modulus E as a function of the imposed penetration depth h_s in the cubic metals ($D = 48$ nm). The critical P_c/E ratio at the onset of defect inception is marked in (b) and (c) along with the associated, normalized first load drop event, $\Delta P/E$. Secondary load drop events, also marked in (a) and (b), become greater in FCC Al than in FCC Cu. A wider variability of the P_c/E ratio is observed in BCC crystals as a function of the assumed atomic potential and surface orientation. (d) Different MD realizations showing the variability of P_c and subsequent contact responses in Fe nanoindentations with $D = 36$ nm. (e) and (f) illustrate the increase of the effective Young's modulus as a function of the indentation pressure (Ta simulations are performed with the potential by Ravelo et al.). The insets show the evolution of the components c_{11} and c_{12} of the elastic stiffness matrix with increasing pressure (see Supplementary Material).

vanishing pressure ($p \to 0$ for $h_s \to 0$). This is in accord with the expected increase in the effective elastic moduli, c_{ij}, at large levels of hydrostatic pressure [39]; which in the current indentation simulations varies depending on the trace of the stress tensor in each material point beneath the surface. This feature is examined here through complementary MD simulations where c_{11} and c_{12} were recorded up to an elevated level of hydrostatic pressure (see the insets to Figs. 1(e) and (f), and the Supplementary Material, S4). For the sake of simplicity, mean values of the effective E within the elastic contact regime were obtained for each surface orientation under an applied pressure which approaches the hardness p_p in Section 3.3. These E values were consistently used hereafter.

Figure 2 shows the evolutions of the mean contact pressure to Young's modulus ratio, p/E, as a function of the normalized contact radius, a/D. The results adhere to the universal linear relationship between p/E and a/D, in accord with the following linear elastic contact mechanics formulations (Ref. [38], Eqs. (4.22) and (4.24)):

$$a = \left(3PD\left(1-\nu^2\right)/8E\right)^{1/3} \tag{2a}$$

$$p = \frac{2}{3}\left(24PE^2/\left(1-\nu^2\right)^2\pi^3D^2\right)^{1/3}, \tag{2b}$$

yielding

$$\frac{p}{E} \approx \frac{0.844}{\left(1-\nu^2\right)}\frac{a}{D}. \tag{3}$$

The good agreement between our simulation results and Eq. (3), see Fig. 2(a)-(d), indicates that the atomic ensembles fulfill coarse-grained, linear elastic contact mechanics [40]. Moreover, since these equations are derived for semi-infinite solids, it is clear that the hardness evolutions are not significantly affected by the boundary conditions imposed to the simulation cells (see Section S1 in the Supplementary Material).

3.2. Summary of early defect inception and critical nucleation pressure

When indented beyond linear elasticity, metallic materials respond with sudden, first pop-in events characterized by different magnitudes of the load drop, ΔP, which mark early defect inception (Fig. 1). Since the material's resistance to defect nucleation and the magnitude of the indentation-induced elastic stress fields both scale with the Young's modulus, E, it follows that an increase in elastic stiffness raises the nucleation pressure p_c. We thus argue that the p_c/E ratio provides an intrinsic measure of the surface resistance to a specific defect nucleation process. The variation of the p_c/E ratio as a function of surface orientation is then governed by the distribution of the slip and twinning systems in which the defects nucleate. Although we here choose to evaluate the surface resistance through far-field contact variables, it is noted that detailed local analyses can be based on molecular mechanics instability parameters (e.g., see [3,41–43]), which account for the pressure hardening effects that would be otherwise neglected when it

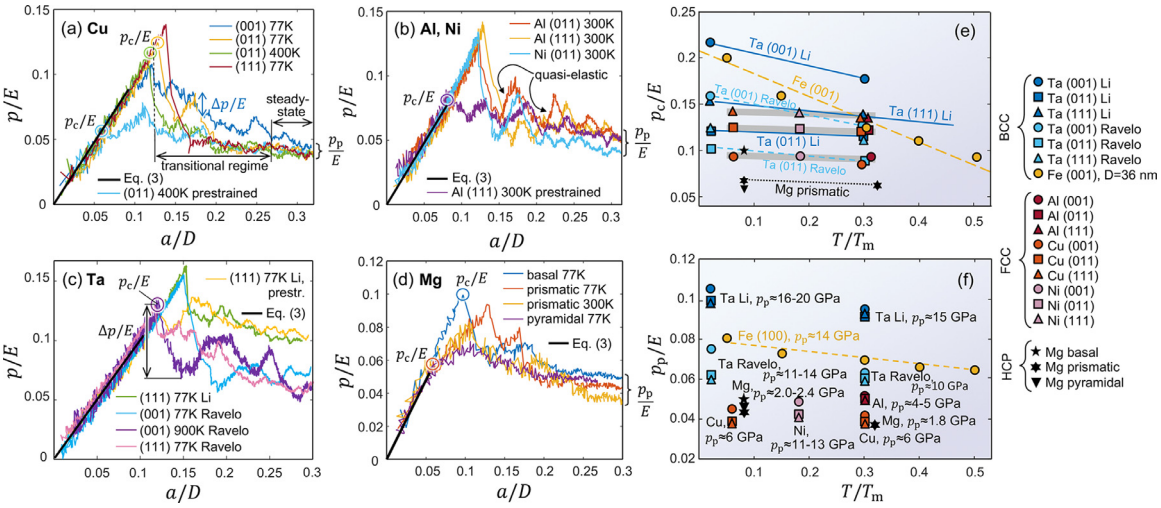

Fig. 2. (a)–(d) Evolution of normalized hardness, p/E, with normalized contact radius, a/D ($D = 48$ nm). It is noted that the increase in hardness with penetration within the early elastic regime adheres to Eq. (3). First pop-ins or plastic instabilities are triggered followed by the onset of the transitional nanoindentation regime, marked in (a). The critical normalized pressure p_c/E triggering early defect nucleation is also marked in the figures along with the associated, first hardness drop, $\Delta p/E$. Notice that the abruptness of the first pop-in varies with crystal structure, surface orientation, and temperature. The normalized, steady-state hardness p_p/E is then indicated in (a), (b), and (d) at the maximum imposed a/D in the simulations. Hardness evolutions with 'prestrained' computational cells containing preexisting defect networks are included in (a)–(c). A summary of the measured p_c/E and p_p/E as a function of the homologous temperature, T/T_m, is provided in (e) and (f), respectively.

is assumed that defect nucleation is uniquely prescribed by a critical resolved shear stress criterion [4,44].

An overview of the p_c/E ratio attained in metal surfaces is given in Fig. 2(e). The associated defect nucleation mechanisms are then illustrated in Figs. 3(a) and 4(a) for FCC and BCC surfaces, respectively, and in Figs. 5(a) and (e) for HCP surfaces. It is remarked that while *different* p_c values attain in FCC Al, Ni, and Cu surfaces indented along a fixed orientation, remarkably *similar* p_c/E result (Fig. 2(e)). This is in accordance with the identical distribution of the slip systems in all FCC surfaces, as well as with the coincidence in the defect nucleation processes which involve the emission of Shockley partial dislocation loops [45,46]. Although the p_c of Ta and Fe are then much higher than those of FCC Al and Cu, this is largely attributed to the higher Young's moduli of the former BCC metals. [Along these lines, it is noted that while similar p_c result in FCC Ni as in the BCC metals because of the large effective E of Ni (which varies from ≈250 to ≈300 GPa depending on the surface orientation), its p_c/E is nearly identical to that in Cu and Al, as described above.]

Although the p_c values are markedly affected by the effective E, our simulation results indicate that the distinct defect mechanisms between the FCC and BCC surfaces still play a clear role in the contact resistance. For instance, our simulations show that the twin emission processes mediated by the nucleation of stacking fault walls in (100) BCC surfaces (see Ref. [4]), render higher p_c/E than the Shockley partial loop nucleation phenomenon observed in all FCC surface orientations (see Fig. 2(e) for $T/T_m < 0.1$). On the other hand, (110) and (111) FCC surfaces exhibit higher p_c/E than similarly oriented BCC Ta counterparts modelled with the potential by Ravelo et al. ($T/T_m < 0.1$). As the same mathematical structure of the stiffness matrix c_{ij} applies to all cubic crystals, these results are indicative in that distinct p_c/E values arise depending on the orientations of the slip and twining systems in which the defects nucleate beneath the surface. Moreover, note that the pressure sensitivity of a given defect nucleation phenomenology may also vary depending on the orientation of the active systems or the employed atomic potential. While comparable twin nucleation processes attain with the different atomic potentials used in the modeling of the higher critical contact pressure levels of BCC metals, the p_c/E ratio is thus reduced by ≈ 30% in the simulations with the potential by Ravelo et al. In the light of the improvements incorporated by this potential in the modelling of high-pressure responses [5], these results are deemed to be more accurate that those obtained with the potential by Li et al.

The MD simulations for HCP Mg render smaller p_c *and* p_c/E than those of the cubic metals, with the exception of the basal (0001) indentations where p_c/E approaches that of the softer (100) FCC surfaces (Fig. 2(e)). This is indicative of the overall greater sensitivity of HCP Mg to the observed basal dislocation loop nucleation processes (Figs. 5(a) and (e)). Along these lines, it is noted that since the resolved shear stress at the basal planes in the subsurface vanishes for $r \to 0$ in (0001) indentations, basal dislocation loops nucleate at a distance from the center of contact ($r \neq 0$), as shown in Fig. 5(a)). Higher values of applied pressure ($p_c \approx 5.1$ GPa) and p_c/E are then measured than for the pyramidal and prismatic surfaces. Moreover, due to the elastic isotropy of Mg, it is argued that the distribution of the basal slip systems beneath the surface exclusively prescribe the measured p_c.

The role of temperature on the measured p_c/E is clearly higher in the harder BCC metals than in the FCC and HCP metals (Fig. 2(e)). Overall, as the temperature increases from cryogenic levels (i.e., from $T/T_m \approx 0.05$ toward 0.3), FCC and HCP metals exhibit a ≈10% decrease in p_c/E while the harder (100) orientations in the BCC metals show a more significant ≈ 20% reduction. As the temperature is further increased to $T/T_m \approx 0.5$, the p_c/E is then reduced by ≈ 50% in (100) surfaces of BCC Fe. Finally, Fig. 6 shows the $P - h_s$ curves and the associated p_c when the indenter tip velocity, v, is reduced from 4 to 0.2 m/s ($D = 100$ nm). While there is a slight variability in p_c when the results of different MD realizations are considered (see Fig. 1(d)), this parameter is consistently decreased by ≈ 10% as the indentation stresses are applied over greater timeframes (i.e., when v is reduced from 4 to 0.2 m/s) [47,48], or when the indenter tip size is increased from $D = 48$ to 100 nm. These results are associated with the occurrence of a greater likelihood for defect nucleation since the number of atomic configurations subjected critical stresses increases for larger simulation timeframes or larger contact radii.

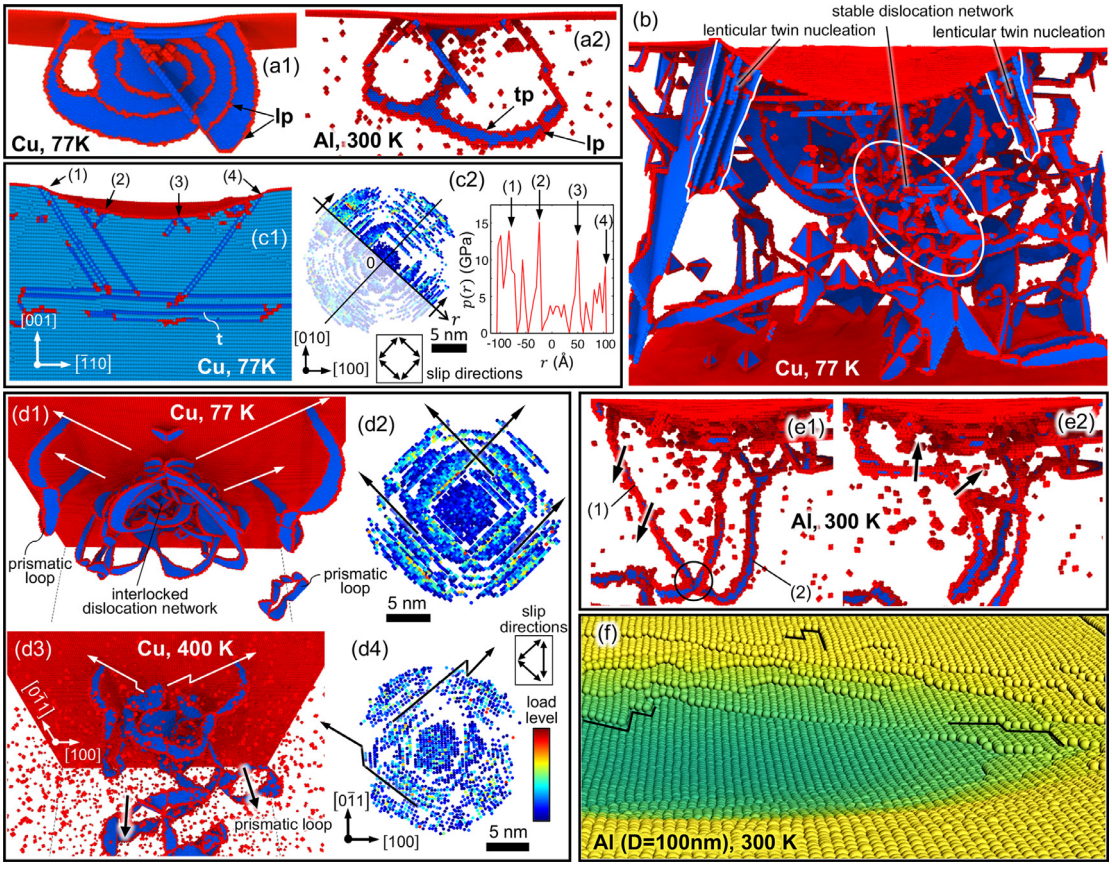

Fig. 3. Imprint formation mechanisms and incepted defect networks in FCC metals. Emission of leading Shockley partial dislocation loops (lp) for (100) indentations is shown in (a1), which is followed by the emission of trailing partial dislocations (tp) in the small stacking fault width Al in (a2). The stacking fault ribbons are marked in blue. The intricate, steady-state defect network attained at large tip penetrations in (111) Cu is shown in (b) along with the prominent, lenticular twins that nucleate at the imprint's rim. Interception of stacking faults and nanotwins beneath the contact in low stacking fault energy Cu is illustrated in (c1), while the associated, serrated pressure distribution produced as the defects emerge at the contact surface is shown in (c2). Increases in temperature favor dislocation cross-slip along with the onset of less developed defect networks; cf. (d1) and (d3) for (110) Cu. The role of elevated temperatures in the load distributions at the contact surface is shown in (d2) and (d4). The revolving of a dislocation segment (1) about its pinning point with segment (2) is shown for (111) Al in (e). The arrows mark the gliding direction of the mobilized dislocation, which is directed towards the imprint in (e2), thus resulting in the emission of a slip trace. Archetypal surface steps from the massive simulations in (100) Al with $D = 100$ nm are illustrated in (f). The slip traces are produced by the glide of screw dislocation segments, where cross-slip occurs upon the constriction of leading and trailing segments, as well as by the interception of dislocation segments in the subsurface; see Supplementary Movie 1.

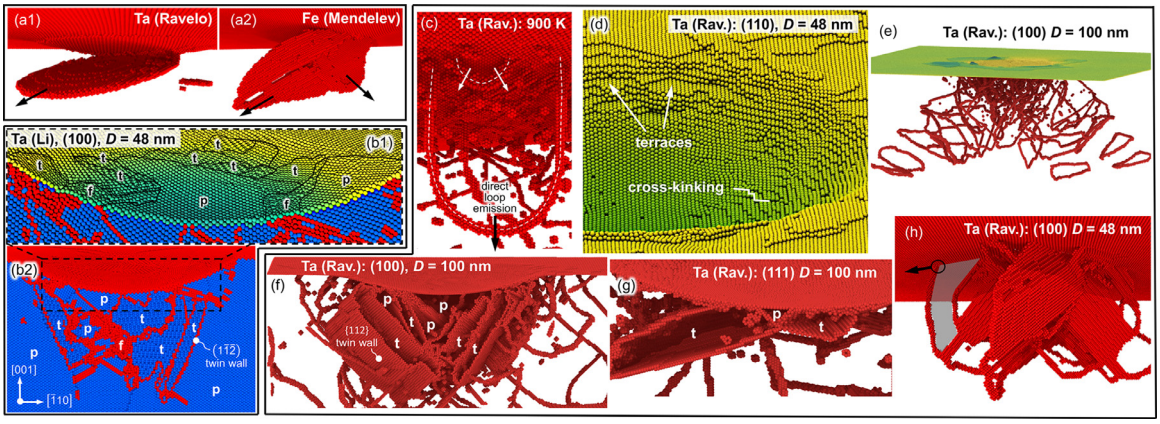

Fig. 4. Imprint formation mechanisms and defect networks in BCC metals indented with $D = 48$ and 100 nm. Early twin nucleation is shown in (a1) for (111) Ta and in (a2) for (100) Fe (arrows indicate the <111> direction of primary twin growth). The nanostructures that develop *via* twin interlocking are shown in (b), (f), and (g) for the two Ta potentials, where parent (p), twined (t), and highly faulted (f) regions are marked; cf. Fig. 7(c). High temperature, direct surface nucleation of a dislocation loop is shown in (c). (d) Cross-kinking of surfaced screw dislocation segments in semicircular paths around the imprint render slip traces and terrace formation; cf. Fig. 3(f) for FCC surfaces. (e) The dislocation network that predominates beneath the surface is observed in a massive simulation with 32 million atoms. (h) Emission of a dislocation loop through twin annihilation (plane marked in grey). The glide direction of the resulting screw dislocation segment at the surface is marked with an arrow.

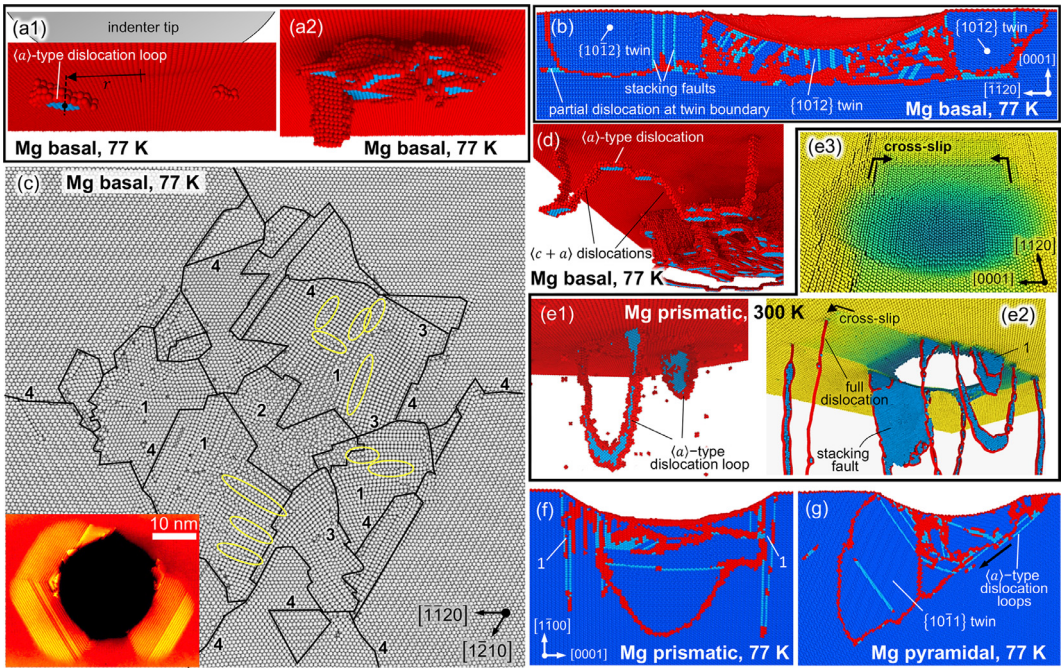

Fig. 5. Imprint formation mechanisms and incepted defect networks in HCP Mg (D = 48 nm). (a) –(c) Defect mechanisms observed in the indentation of basal surfaces. Early nucleation of <a>-type dislocation loops at finite distance r from the center of contact is illustrated in (a1), leading to the onset of the defect arrangement in (a2). (b) Cross-sectional view of the incepted nanograin substructure, composed of the marked tensile 10$\bar{1}$0 and compressive 10$\bar{1}$1 twins. Stacking faults are shown in pale blue. (c) Top view of the indented plane, which highlights the subgrain structure (1), the highly-faulted central region (2), and dislocation tilt (3) and coherent (4) twin boundaries. Edge dislocations are marked in yellow. (d) Surface slip traces are produced through a particular dislocation configuration where dissociation into <c+a> dislocations is observed. (e)–(g) Defect mechanisms in the indentations of the prismatic and pyramidal planes. Recurrent nucleation of <a>-type basal dislocation loops at the contact rim –marked "1" in (e2) and (f)– produces a dislocation arrangement where the constriction of leading and trailing dislocation partials results in the onset of full screw dislocation segments. Cross-slip of these segments leads to the slip trace arrangement in (e3). (f) and (g) Details of the interlocked grain substructure developing beneath the surface *via* twin emission along with <a>-type basal dislocation loops.

3.3. Imprint formation mechanisms and the evolution toward steady-state nanocontacts

Nanoimprint formation occurs during the first and subsequent secondary pop-in events or plastic instabilities *via* the defect mechanisms in Figs. 3-5 and 7. As defect nucleation and defect remobilization processes abruptly occur beneath the surface, a reduction in the magnitude of the vertical displacement field for a given radial distance, $\Delta u_z(r)$, develops at the contact surface (Fig. 7(f)). The total applied load is then decreased by an amount ΔP. Increases in the displacement u_r at the contact rim ($r = a$) also occur, which lead to a sudden raise in the contact area, A, and in the pileup parameter, c^2 (Fig. 7(a-d)). This results in greater pressure drops, Δp, than the associated load drops themselves.

Figs. 2 and 6 show the development of a transitional indentation regime following the first pop-in event. This regime is characterized by the onset of quasi-elastic indentation loading stages, where pronounced increases in hardness occur (denoted with a large slope dp/dh_s in Fig. 6(b)) followed by secondary hardness and load drops. These instabilities are produced by defect remobilization or abrupt imprint formation processes, resulting in increasingly stable lower hardness states or contact configurations. The extent of the transitional regime varies with crystal structure and surface orientation, as it is prolonged in FCC Al as well as in (100) BCC Ta surfaces modeled with the potential by Ravelo et al. where large plastic instabilities continue to occur for $a/D = 0.3$ (Fig. 2).

Self-similar steady-state nanoindentations are finally instated, as distinguished by smaller plastic instabilities (i.e., small Δp values) which denote the attainment of more gradual imprint formation processes (Fig. 6(b)). A plateauing, mildly decreasing hardness p_p is then reached (as measured here at $a/D \approx 0.3$) under rather constant dislocation density ρ_p (Figs. 2, 6 and 8), thus resembling the hardness evolutions from self-similar continuum plasticity analysis of weak strain hardening metals [49,50]. These results suggest that a robust balance between the imprint formation processes and the strengthening provided by the entangled defect network in the cubic metals develops passed the first few pop-in events. This leads to increasingly stable contact configurations where the collective defect processes are gradually hindered ($a/D > 0.20, h_s \approx 4$ nm and $D = 100$ nm).

The occurrence of steady-state nanoindentations is attendant on the transition from the early elastic contact response, where marked 'sinking-in' develops ($c^2 \to 0.5$), to a conforming contact configuration where the indenter tip is encased at the surface while 'pileup' effects occur at the imprint's rim ($c^2 \to 0.8–1.0$); Fig. 7. Material pileup is concomitant with the emission of slip traces and twins at the surface [29], so that the pressure distributions become discontinuous or serrated (cf. Fig. 7(a) with Fig. 3(c)).

Upon the onset of conforming nanoimprints, smaller radial displacements (Δu_r) develop throughout the contact rim ($r = a$) when the indenter tip is removed from the surface. The area of the residual imprint thus approaches the true contact area under the applied load, suggesting that the experimentally measured hardness (H) approximates to the mean contact pressure (p). On the other hand, within the early transitional regime where marked sinking-in still develops ($c^2 < 1$), indenter tip unloading leads to a significant Δu_r which increases the apparent contact area, so that $H < p$ (see Supplementary Material).

Our simulation results are pertinent to the interpretation of nanoindentation size effects [51], where a steady decrease in hardness is observed with increasing tip penetration. While different mechanisms account for these size effects depending on the length scale which governs the indentation process, it is emphasized that the current MD simulations concern the extreme hardness levels

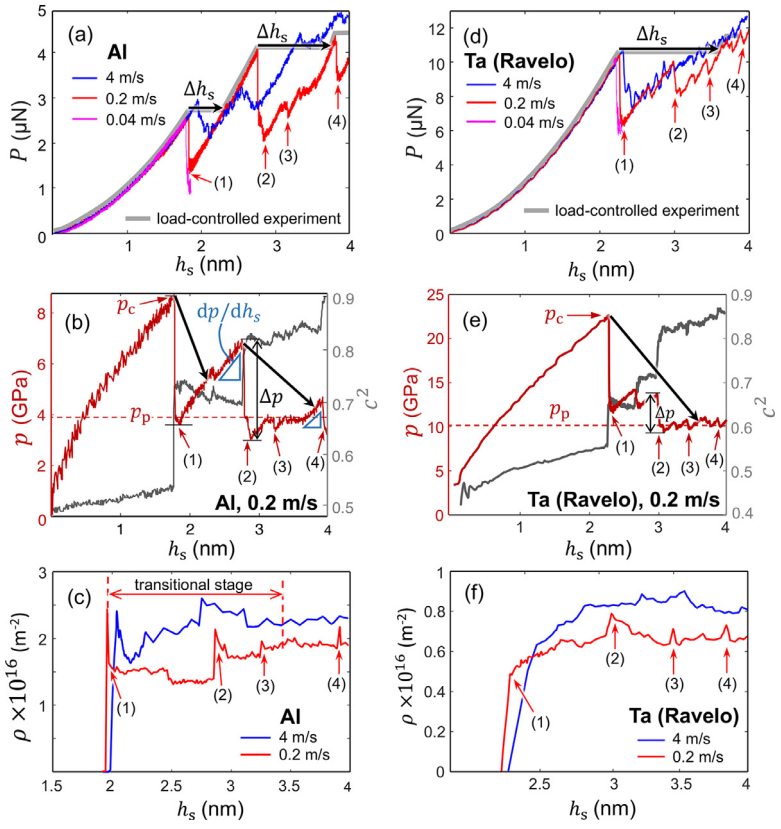

Fig. 6. Load and hardness evolutions with tip penetration from massive MD simulations performed with an experimentally realistic indenter tip diameter $D = 100$ nm at $v = 0.04$, 0.2 and 4 m/s in (100) FCC Al (a)–(c), and in (111) BCC Ta (d)–(f) modeled with the atomic potential by Ravelo et al. The load–penetration depth (P–h_s) curves in (a) and (d) show the load drop events associated with defect nucleation and remobilization. The figures contain the anticipated P–h_s curves (in grey) from nanoindentation experiments performed with dynamically-reactive testing systems that operate under load control (see Section 3.5) along with the associated strain bursts, Δh_s. Note that the magnitude of the load drops increase with decreasing indenter velocity, v, as discussed in the main text. The hardness drops and associated strain bursts are then plotted in (b) and (e) along with the evolution of the pileup parameter c^2. The evolutions of the dislocation density, ρ, within the incepted defect networks are shown in (c) and (f). Note that a decrease in ρ is observed when the penetration velocity is reduced. See text for further details.

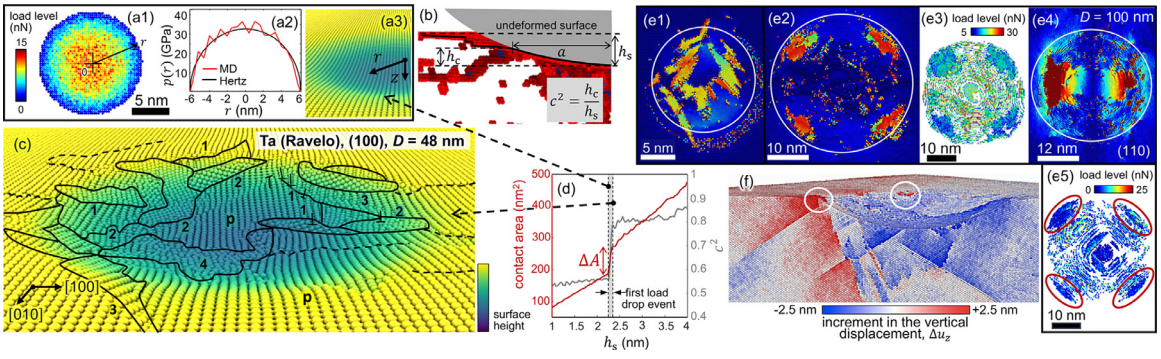

Fig. 7. Nanoimprint formation in BCC Ta (simulations with the potential by Ravelo et al. for (100) surfaces with $T = 77$ K and $D = 48$ nm). (a) Incipient elastic (Hertzian) load (a1) and pressure (a2) distributions along with the contact surface attained prior to the first pop-in event (a3). The tip penetration depths h_s and h_c are shown in (b), which are used in the calculation of the pileup parameter $c^2 = h_c/h_s$. The permanent nanoimprint that is subsequently formed upon the termination of the first load drop is displayed in (c), where the associated raise in contact area and in c^2 is marked in (d). The nanostructure produced across the imprint in (c) is comprised of semicoherent dislocation boundaries (1), incoherent boundaries (2), coherent boundaries (3), and highly faulted regions (4); "p" denotes the parent crystal lattice orientation and the discontinuous lines mark slip traces (see Supplementary movie 2). The nanostructure and individual crystallites at the contact area are revealed in (e1) and (e2) through the local lattice orientation patterns, see Ref. [71] (white circles indicate the imprint's rim). The load distribution which corresponds with the penetration depth in (e2) is given in (e3). The figure shows load concentration at the slip traces as well as four-fold symmetrical crystallites. The load distribution resulting in (100) FCC Cu surfaces is shown in (e5); where the regions with a rather homogeneous, concentrated load distribution (marked in red) are associated with lenticular twin nucleation. This concentrated load distribution resembles that from the BCC crystallites in (e3). The nanograins or crystallites emerging in (110) BCC Ta surfaces indented with $D = 100$ nm are further shown in (e4). (f) Atomic displacement produced during a secondary plastic instability (Ravelo potential). The color code indicates that the atoms at the imprint are displaced downwards (blue) due to the slip carried by defect glide in the subsurface. Notice that local pileup effects (highlighted with white circles) develop at the imprint's rim, which contributes to imprint formation.

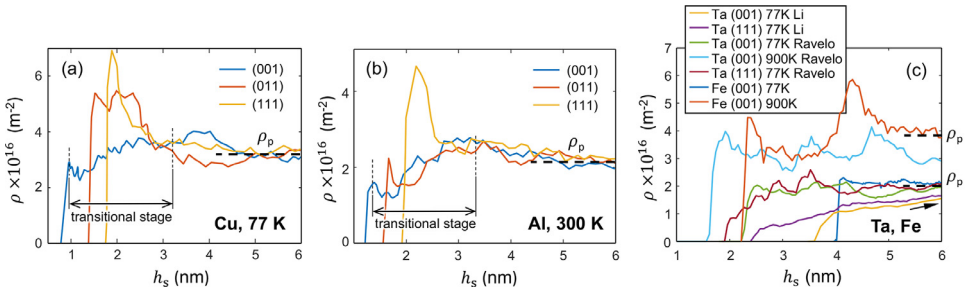

Fig. 8. Evolution of the dislocation density, ρ, in FCC (a,b) and BCC (c) crystals from the simulations with $D = 48$ nm and $v = 4$ m/s. Past the early defect nucleation process where the dislocation density abruptly increases, the overall results in (a) and (b) show the gradual vs. the more abrupt attainment of the plateau, steady-state density ρ_p (see text for details). In the case of the BCC surfaces in (c), a dislocation network is incepted through twin annihilation processes, which varies depending on surface orientation and atomic potential. Increases in temperature then result in greater values of ρ_p, as twin annihilation is favored.

reached in *low-load* nanoindentation experiments where the penetration of a blunt, nanoscopic tip triggers specific imprint-forming processes as a function of crystal structure, temperature and orientation, as described next.

3.3.1. FCC metals

Nanoimprint formation in FCC metals involves: (i) recurrent dislocation loop nucleation processes from the surface that render slip trace emission (Fig. 3(d)); (ii) collective glide of the surfaced *screw* dislocation segments in small stacking fault width Al (Fig. 3(f)), as well as the interaction of stacking faults and twins that produces sharp zig-zagging slip traces in metals with large stacking fault width; (iii) thickening of the incepted lenticular twins at the imprint's rim, markedly enhancing pileup effects and the development of well-defined nanoimprints in large stacking fault width Cu and Ni (Fig. 3(b)); (iv) revolving of dislocation segments around junction nodes at the plastic zone which finally results in dislocation emission at the imprint (Fig. 3(e)). The active slip systems in the simulations are always of the $\{111\}\langle\bar{1}10\rangle$ family, even though short range cross-slip processes in FCC Al are found to produce complex slip trajectories which, in overall, do not appear to lie within a unique crystallographic plane.

During the transitional indentation regime, the occurrence of secondary pop-ins is associated with the sudden expansion of pinned dislocation loops, which leads to the remobilization of an increasing number of dislocation segments in a collective, avalanche type response. Following the attainment of the first pop-in event, defect network buildup occurs along with a steady increment of the dislocation density ρ (Figs 8(a) and (b)). The transitional regime however vanishes when larger *first* load drop events occur, as in (111) indentations. This is associated with abrupt defect interaction and interlocking, which hardens the surface and facilitates the onset of the steady-state. Further increases in tip penetration are then accommodated through local rearrangements of the defect structure under rather constant, plateau dislocation density ρ_p. As highly entangled FCC networks with large stacking fault ribbons hinder dislocation remobilization, less prominent plastic instabilities occur beneath the surface of Cu and Ni under a higher ρ_p than in Al.

Smaller ρ values develop when the penetration velocity decreases from $v = 4$ to 0.2 m/s in (100) Al surfaces indented with the larger tip diameter, $D = 100$ nm (see Fig. 6(c)). More prominent defect nucleation and remobilization processes are also observed for $v = 0.2$ m/s, leading to greater ΔP and Δp (Figs. 6(a)) along with a smaller p_p. This suggests that while there is an increased likelihood for the emission of larger dislocation avalanches when the less interlocked Al networks are subjected to the contact pressure over greater timeframes, increases in penetration velocity result in more entangled networks as cross-slip is tentatively hindered. Our results also show that smoother hardness evolutions occur in Cu surfaces indented at elevated temperature, whereas more prominent avalanches develop at cryogenic temperatures (Fig. 2(a) for Cu (011)). As the secondary pop-ins are thus triggered at smaller applied pressure levels at elevated temperature due to the enhanced mobility of the defect network, the magnitudes ΔP and Δp of the load and hardness drops are consequently reduced.

Since the applied contact pressure or hardness p_p scales with the Young's modulus, the p_p/E ratio emerges as a relevant dimensionless index for the comparison between the nanocontact plasticity mechanisms in metals with distinct elastic properties (see Fig. 2(f)). [Along these lines, it is noted that since dislocation remobilization occurs at smaller stresses in metals with lower elastic moduli, the hardness p_p would then be potentially decreased while the value of p_p/E ratio is arguably maintained.] Our simulation results show that the p_p/E ratio becomes clearly *smaller* in Cu and Ni than in Al surfaces, in spite of the much higher hardness p_p of the former. While the hardness of Cu and Ni is enhanced by the occurrence of highly interlocked defect networks with large stacking fault ribbons, prominent emission of lenticular twins facilitates nanoimprint formation along with a reduction in the p_p/E ratio. Our simulations inadvertently contrast with experimental findings from greater micrometer-sized indentations ($D \approx 200$ μm; $a/D \approx 0.3$), where the hardness to Young's modulus ratio of Cu would be *twofold greater* than in Al [52] due to the pronounced dislocation cross-slip and smaller ρ in the latter [53]. This apparent discrepancy points to the fact that in the nanoscale, imprint formation *via* surface lenticular twin emission effectively reduces the hardness of metals with large stacking fault width, while this imprint-forming mechanism is indeed absent in greater micrometer-sized indentations where the hardness is governed by dislocation-mediated plasticity at much smaller yield stresses (see Section 3.4).

3.3.2. BCC metals

Nanoimprint formation in BCC metals involves: (i) inception of nanostructured subgrain arrangements or crystallites (Figs. 4(b), (f) and (g)); (ii) nucleation of lenticular twins which are then potentially annihilated, leading to dislocation loop emission (Fig. 4(h) and Ref. [4]); (iii) direct dislocation loop nucleation at the imprint (Fig. 4(c)); and (iv) cross-kinking of surfaced screw dislocations, producing semicircular slip traces (Fig. 4(d)). The preferential slip system families are of the $\{11\bar{2}\}\langle111\rangle$ and $\{01\bar{1}\}\langle111\rangle$ types.

The indentation of (100) Ta surfaces, modeled with the potential by Li et al., exhibits the highest nucleation pressure p_c. This higher, critical contact pressure triggers recurrent twin nucleation throughout the first load drop event, resulting in the interlocked nanostructures with impinged subgrains in Fig. 4(b). The incepted nanostructures are comprised of primary twins, secondary twins nucleated at {112} boundaries, parent material regions, and highly defective zones (Figs. 7(c) and (e(1)). Substructural refinement then

occurs through dislocation processes and twin boundary migration. Crystallite interlocking is less marked in (111) and (110) surfaces, where smaller p_c attain, than in (100) surfaces. While less-developed nanostructures then arise under the relatively milder p_c from the simulations with the potentials by Ravelo et al. for Ta and Mendelev et al. for Fe, increases in indenter diameter to $D = 100$ nm in all Ta surfaces (Figs. 4(f) and (g)) lead to the inception of thicker twins or crystallites and to a similar substructural development as in the simulations with the potential by Li et al. Such *in situ* nanostructural development suggests a similitude between the indentation response of single crystals and that of the nanostructured polycrystals in Refs. [54–56].

Since a smaller applied pressure is reached passed the first pop-in event with the potentials by Ravelo et al. and Mendelev et al. ($D = 48$ nm), detwining is observed *via* dislocation activity at the {112} boundaries, which annihilates the subgrain structure. This feature is enhanced in the elevated temperature simulations. Nevertheless, when D is increased to 100 nm (Ravelo et al.), the coarser subgrains incepted with such experimentally realistic tip sizes (Figs. 4(g), 4(h), and 7(e(4)) become fully stable. It is noted that in spite of the nanostructural annihilation that develops with the potential by Ravelo et al. for $D = 48$ nm, individual twins or crystallites with rather equiaxial shape nucleate at the outer regions of the imprint subjected to high shear stresses ($a/D \geq 0.2$), forming four-fold rotational symmetry patterns in (100) surfaces (Fig. 7(e2)). The hardness evolution is then governed by the critical applied pressure under which abrupt, crystallite expansion occurs at the imprint's rim ($r = a$). This leads to the recurrent secondary pop-in events and extended transitional regimes in (100) Ta (Fig. 2(c)).

Further permanent imprint formation develops in all Ta surfaces through collective glide of screw dislocation segments along semicircular paths (Fig. 4(d)). This leads to the formation of surface steps that trace the indenter tip under a steady hardness (constant dp/dh_s). While load concentration is observed at the surface steps, the contact load potentially vanishes at the terraces (Fig. 7(e3)).

The thermally-assisted nature of the defect processes in BCC metals is evidenced from our simulation results. It is noted that while the overall plasticity mechanisms prevail when the temperature increases from 77 K to 900 K in the Ta simulations (Ravelo et al.), highly recurrent twin nucleation and annihilation as well as direct dislocation loop nucleation events at the surface are observed. This renders higher ρ_p (Fig. 8(c)), greater hardness drops, and smaller p_p/E (Fig. 2(c) for (100) Ta). The lowering of p_p at elevated temperature is however milder for the relatively softer (110) and (111) Ta surfaces (Ravelo et al.), where the magnitude of the secondary load drops is also reduced. Finally, a decrease in indenter velocity v to 0.2 m/s (D =100 nm, Ravelo et al.) leads to a ≈15% reduction in p_p. While more prominent secondary load and hardness drops are then observed as twin annihilation is promoted for $v = 0.2$ m/s (Fig. 6(d)), dislocation network entanglement is slightly reduced (Fig. 6(f)) as cross-kinking is also tentatively enhanced.

3.3.3. HCP Magnesium

The imprint formation mechanisms in basal, prismatic and pyramidal Mg surfaces are illustrated in Fig. 5. Indentation of basal (0001) surfaces leads to the nucleation of $\langle a \rangle$-type dislocation loops (Fig. 5(a)). A nanostructured, highly-interlocked subgrain arrangement then develops within the first pop-in event, which sustains the larger indentation-imposed strain along the c-axis (Fig. 5(b)). The incepted substructure consists of tensile $\{10\bar{1}2\}\langle\bar{1}011\rangle$ and few compressive $\{10\bar{1}1\}\langle10\bar{1}\bar{2}\rangle$ twinned crystallites, which contain stacking faults, along with highly defective regions. The interfaces comprise dislocation tilt and coherent boundaries (Fig. 5(c)). Slip trace emission is associated with the glide of a peculiar dislocation configuration comprised of basal $\langle a \rangle$ and pyramidal $\langle c + a \rangle$ segments (Fig. 5(d)). While the highest critical pressure attains in (0001) surfaces where the basal planes are parallel to the indented surface ($p_c \approx 5.1$ GPa, Fig. 2(e)), greater secondary hardness drops are also detected with increasing tip penetration along with the development of the nanostructured region throughout the imprint.

During the indentation of prismatic surfaces, recurrent nucleation of dislocation loops at the basal planes is observed (Fig. 5(e1), (e2) and (f)), resulting in slip trace emission in $\langle 11\bar{2}0\rangle$ directions (Fig. 5(e3). This contributes to imprint formation by facilitating the onset of pileup effects in each pop-in event. While the nucleation of leading dislocation partials produces stacking fault bands in the RT simulations (marked "1" in Fig. 5(f)) along with the onset of secondary hardness drops, the nucleation of trailing partial dislocations is promoted at elevated temperature thus preventing large staking fault band formation (Fig. 5(e2)). As the leading and trailing partials glide, segment constriction develops which facilitates cross-slip events toward the intercepting prismatic planes. This produces distinct, zig-zagging slip traces (Fig. 5(e2) and (e3)). Tensile $\{10\bar{1}2\}\langle\bar{1}011\rangle$ twins are also detected beneath the surface, where the intricate nanostructure reported in the (0001) basal indentations is lacking (cf. Figs. 5(b) and (f)). Finally, the indentation of pyramidal surfaces is characterized by the nucleation of basal dislocation loops at the contact rim (Fig. 5(g)). This mechanism is favored under the large resolved shear stress acting on the basal planes, which renders the smallest critical pressure ($p_c \approx 2$ GPa) along with vanishing hardness drops. A less intricate arrangement of $\{10\bar{1}2\}\langle\bar{1}011\rangle$ and $\{10\bar{2}1\}\langle\bar{1}\bar{1}26\rangle$ crystallites is also observed (cf. Figs. 5(b) and (g)).

Our results show that the greater pop-ins attained in the indention of basal surfaces are due to the evolution of the nanograin substructure which promotes imprint formation. While basal indentations exhibit the highest p_c, the more pronounced substructural evolution observed for this orientation results in a steady-state p_p that approximates to those from the other orientations. Finally, it is found that the glide of the incepted, basal dislocation loops occurs without significant interaction beneath the surface. This precludes the development of the entangled defect networks observed in cubic metals. [Enhanced dislocation interactions may however occur when D decreases to ≈5 nm [27]].

3.4. Correlation between the nanohardness and the yield strength

The correlation between the hardness and the uniaxial yield stress of the indented material has been extensively examined on the basis of continuum elasto-plastic contact mechanics (e.g. [38]). In spherical indentation, the hardness to yield stress ratio, p/σ_{ys}, is known to increase with tip penetration from the limiting value of ≈ 1.1, where plastic yielding commences at a distance $z = 0.5a$ beneath the center of contact, to the upper fully-plastic bound of $p/\sigma_{ys} \approx 2.8$ [38,49]. While the von Mises stress field is centered below the contact surface according to elasticity, this feature is lost with the advent of plasticity where the maximum von Mises stress shifts toward the surface while the extension of the plastic zone spreads outward from the center of contact [49].

Our results indicate that while the von Mises stress field in the early elastic regime indeed becomes maximum beneath the surface (at $\approx 0.5a$, Fig. 9(a1) and (b1)), its axial symmetry is strictly lost due to elastic anisotropy. The p/σ_e ratio at the location of the maximum von Mises stress is then found to vary within ≈ 1.2 to 1.5 depending on the orientation of the indented crystal, which is higher than the value of 1.1 asserted on the basis of elastic isotropy. Upon the onset of plasticity, superposition of the individual stresses carried by the dislocations to the indentation-induced stress field results in local peaks of the von Mises stress, which become increasingly noticeable during each successive plastic in-

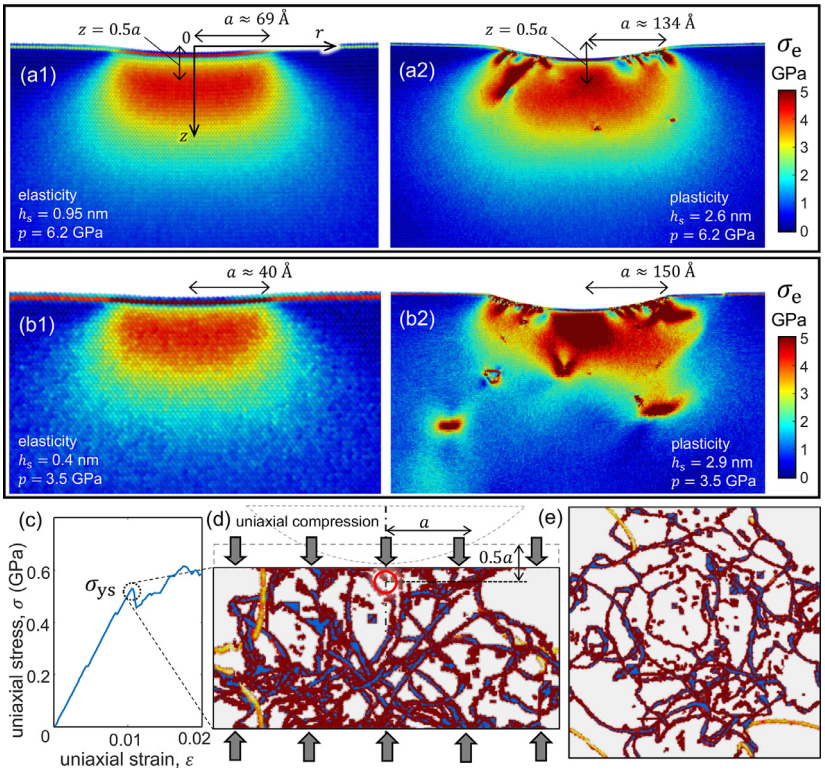

Fig. 9. Stress fields and dislocation mobilization events within the defect network in (100) Al (D = 100 nm, v = 0.2 m/s). The von Mises stress (σ_e) fields within the early elastic contact response are shown in (a1) and (b1). Upon early defect inception, the von Mises fields (a2 and b2) show stress concentrations at the incepted dislocation lines. Since tip penetration occurs under decreasing applied pressure or hardness, the von Mises fields in (a2) and (b2) are consistently drawn for the same values of imposed pressure as the elastic contacts in (a1) and (b1). The mobilization of the dislocation networks present in steady-state indentations when subjected to *uniaxial compression* is illustrated in the side view (d), and in the top view (e). The dislocation segments that activate at $\sigma = \sigma_{ys}$, far away from the center of contact are highlighted in yellow. The corresponding uniaxial stress−strain curve is shown in (c). If the prestrained MD cell would have been subjected to contact loadings, dislocation remobilization would occur at $z = 0.5a$ according to continuum plasticity analyses, as marked in (d). Note that since the material at this location is potentially dislocation free, a fundamental basis is lacking for these continuum plasticity predictions (see Section 3.4).

stability (cf. Figs. 9(a2) and (b2)). As the dislocations glide and interact, the magnitude of the von Mises stress is incremented immediately beneath the surface due to the buildup of radial stresses, which enhance pileup effects.

The contact response in the nanoindentation simulations defies continuum plasticity analyses for solids with *continuous* dislocation distributions, where plastic straining is enabled in *all* locations beneath the surface. In the indentation simulations with the 'prestrained' cells containing steady-state networks, it is then found that (i) the critical region where plasticity would be expected to initiate ($r = 0,\ z = 0.5a$) remains dislocation starved (Fig. 9(d)), (ii) the mobilized dislocation segments lie within mildly interlocked regions of the network, which are located away from the center of contact where the von Mises stress is maximum (Fig. 9 (e)) and (iii) the defects at the plastic zone are clearly embedded in an *elastic* stress field.

Interestingly, it is found that while continuum plasticity does not apply to the current nanocontacts, the strain hardening relation $\tau_c = \alpha G b\sqrt{\rho} = \sigma_{ys} \times$ SF, where τ_c is the critical resolved shear stress, G is the shear modulus, b is the magnitude of the Burgers vector and SF is the Schmid factor, accurately predicts the σ_{ys} in our uniaxial simulations with the 'prestrained' cells that contain the indentation induced, steady-state dislocation network. The dislocation interaction coefficient α then approaches 0.3, in good accord with continuum crystal plasticity estimates. Although the coarse-graining of dislocation-mediated plasticity is thus pertinent to the analysis of plastic yielding under uniform strain, the expansion of the plastic zone at large strain gradients eludes such continuum theories as the assumption of a continuous variation in dislocation density is violated.

In spite of the above observations, an attempt to correlate the uniaxial response with the measured hardness can be based on the MD simulations where the 'prestrained' cells where subjected to a further indentation loading stage, as well as to an externally applied homogeneous strain (Section 2). The values of the p_p/σ_{ys} ratio then become ≈ 7 and ≈ 8 in FCC Al and Cu, respectively, and ≈ 10 in BCC Ta (see Table 1), strongly exceeding the continuum mechanics *upper* bound of $\approx$2.8 [38,49]. In these analyses, it is noted that the uniaxial yield stress in the MD simulations is marked by the onset of a collective dislocation avalanche type response in the sense described in [57]. Moreover, as strain hardening is already saturated due to the preexisting large dislocation density, this feature is inconsequential to the measured σ_{ys} (see Section S5 in Supplementary Material).

Since the p_p and steady-state network topologies reached with defect-free MD cells are equivalent to those from the 'prestrained' cells (Fig. 2), it is argued that the p_p/σ_{ys} ratio provides a fundamental assessment to the nanoindentation response of metal surfaces. This ratio thus correlates the uniaxial and contact responses of heavily strained metals containing the characteristic highly entangled defect networks present in steady-state nanoindentations. In this correlation, a clear inconsistency is however evidenced between the substructural evolutions rendering nanoimprint formation under large applied pressure (Sections 3.3.1-3.3.3) and the specific dislocation mechanisms attained at the plastic zone. In this sense, it is emphasized that while the latter include the devel-

Table 1
Hardness $\boldsymbol{p_p}$ and corresponding yield strength $\boldsymbol{\sigma_{ys}}$ of steady-state nanocontacts.

	$\boldsymbol{D}$ (nm)	$\boldsymbol{T}$ (K)	$\boldsymbol{\sigma_{ys}}$ (GPa)	$\boldsymbol{p_p}$ (GPa)	$\boldsymbol{\rho}$ ($\mathbf{m}^{-2}$)*	$\boldsymbol{p_p/\sigma_{ys}}$
Ta (001) Li et al.	48	300	1.65	≈18.0	1.6×10^{16}	10.9
Ta (001) Ravelo et al.	48	300	1.20	≈12.2	1.9×10^{16}	10.2
Cu (011)	48	400	0.80	≈6.5	3.1×10^{16}	8.1
Al (001)	100	300	0.56±0.03 (‡)	≈3.9	1.9×10^{16}	7.4
Al (011)	48	300	0.65	≈4.5	2.1×10^{16}	7.0

* $\boldsymbol{\rho}$ is the dislocation density of the defect networks incepted through the indentation simulations. These networks are then remobilized upon subsequent *uniaxial* straining. The reported yield strength is the mean value from 3 different MD realizations. The indentation orientation indicated in the first column coincides with that along which the subsequent uniaxial strains were applied. In the case of the simulations of (100) Al surfaces, the uniaxial strains were applied along the three <100> orientations, which yielded the reported mean $\boldsymbol{\sigma_{ys}}$ (‡).

opment of multi-segment nodes −where various dislocation lines converge at a single point− along with dislocation unzipping and recurrent stacking fault interception, nanoimprint formation in FCC and BCC metals is particularly affected by the nucleation of lenticular twins and crystallites.

Finally, note that the current p_p exceed hardness measurements from micrometer-sized spherical tips, where even upon the onset of significant indentation size effects, imprint formation complies with the postulates of continuum dislocation-mediated plasticity [50,52,53,58]. These microscale imprints are thus amenable to analysis through size-dependent continuum plasticity theories which do not apply to the present nanocontacts.

3.5. Comparison between MD simulations and experiments

3.5.1. P-h_s curves and hardness evolutions

The critical pressure, p_c, triggering defect inception can be estimated when the pop-in load, P_c, is inserted into Eq. (2b). Since surface steps and preexisting dislocations produce a large variability of the inferred nucleation pressure in nanoindentation experiments, the *intrinsic* p_c from the MD simulations represents an upper mechanical bound. Along these lines, the maximum $p_c \approx 7.0$ GPa inferred by Shibutani et al. [14] from their experiments in a (100) Al surface is thus ≈ 20% smaller than the value of $p_c \approx 8.5$ GPa from our RT simulations. This difference is slightly increased in (100) Cu surfaces, where the experimentally assessed $p_c \approx 7.6$ GPa, while the simulations render $p_c \approx 11.2$ GPa.

A systematic investigation on the variability of the critical pressure was performed by Lawrence et al. [59] in (100) Ni, where the value of $p_c \approx 24$ GPa from our RT simulations matches the maximum inferred pressure from the pop-in distribution measured in the experiments with the smaller tip diameter of $D \approx 200$ nm. It is noted that the maximum p_c in this distribution is reduced by half as the indenter tip diameter is increased to $D \approx 650$ nm, which is associated with the greater likelihood for preexisting dislocations to lie within the strained volume. This interpretation is consistent with our simulation results, where 'prestrained' computational cells containing a dislocation arrangement exhibit a drastic ≈ 50% reduction in p_c (Fig. 2(b)). Concerning BCC Ta, the current p_c of ≈ 29 GPa for (100) surfaces (Ravelo et al.) is fully consistent with the highest experimentally measured P_c reported in Fig. 2 from Biener et al. [60].

When comparing experiments with MD simulations, it is important to consider that the former are conducted with dynamically reactive systems which produce the rapid acceleration the indenter tip onto the surface upon the onset of the first pop-in event [57]. This leads to a plastic burst of magnitude Δh_s (as illustrated in Figs. 6(a) and (d)). Since measurements of the applied load P are inhibited during a dynamically-driven plastic burst, the ultrafast secondary load drop events that develop in the MD simulations over minuscule time scales of ≈ 0.1 ns remain concealed in the experiments [57]. To evaluate the projected contact area upon *strain burst termination*, we employ the c^2 from our simulation results at the same h_s/D ratio as in the experiments. Upon the onset of the first pop-in event, the hardness inferred from the experiments by Shibutami et al. in (100) Al and by Franke et al. in (111) Ta then become $p \approx 5.3$ and 9.5 GPa, respectively. While the latter value is maintained during subsequent strain bursts, thus approaching the range of p_p levels from our simulations, the former is slightly reduced and thus approaches the simulated value of $p_p \approx 4.5$ GPa (Figs. 6(b) and (e)). Finally, the experiments by Shibutami et al. show the occurrence of greater secondary strain bursts in Al than in Cu, which is also in accord with the greater Δp and ΔP values from our simulations in Al (Fig. 2).

Concerning HCP Mg, the applied pressure levels of ≈ 5.5 GPa and ≈ 4.2 GPa which mark *abrupt* defect inception in the nanoindentation experiments of basal and prismatic surfaces by Somekawa et al. [61] are in agreement with the values of ≈ 5.1 GPa and ≈ 4.0 GPa attained in our MD simulations at the onset of the first pop-in event. Along these lines, the simulations show that a gradual departure from perfect elasticity occurs in prismatic and pyramidal surfaces (Fig. 2 (d)), which is also in accord with the results by Somekawa et al. and by Catoor et al. [62]. This feature is due to the progressive inception of defects −as opposed to the abrupt defect nucleation phenomena observed in the basal surfaces− and is thus used to estimate the effective p_c in Fig. 2. By considering the currently measured c^2 for steady-state indentations of HCP Mg, the inferred p_p from the experiments by Somekawa et al. become ≈ 2.9 GPa and 2.5 GPa for basal and prismatic surfaces, respectively, which approach our simulation results of ≈ 2.5 and 2.1 GPa.

3.5.2. Defect mechanisms

Experimental support for the key role of the screw dislocations and cross-slip on the onset of pileup effects is given in [63,64]. In a similar vein, transmission electron microscopy (TEM) in conjunction with electron backscatter diffraction (EBSD) analyses have provided detailed characterizations of the entangled dislocation networks developing in *greater* nanoindentations of FCC single crystals along with maps of the GND density [65,66]. While the currently observed deformation twinning is hindered in these experiments even at cryogenic temperatures [67,68], the simulation results concern smaller nanoimprints where the larger shear strain gradients and stresses at the contact surface trigger substantial twinning processes, as evidenced in the MD analyses of FCC Cu and Ni.

In the context of the defect mechanisms reported in HCP Mg, the work by Catoor et al. supports that early defect nucleation is indeed associated with the inception of $\langle a \rangle$-type dislocations in basal planes (rather than in prismatic planes), followed by the emergence of $\langle c + a \rangle$ dislocations. While deformation twins were detected in the TEM foils extracted from larger imprints, this de-

formation mode is more pronounced in the Mg *micro*indentations assessed through EBSD analyses by Zambaldi et al. [69], where multiple twin lamellae developed around these greater imprints. These findings are fully compatible with the currently observed nanostructures (inset to Fig. 5(c)). The TEM analyses by Somekawa et al. concerning smaller nanoimprints also show the occurrence of marked defect dissemination throughout the thickness of the crystal with little dislocation accumulation beneath the contact surface, in agreement with our MD simulations. Moreover, the evolution of the nanograin substructure in (0001) surfaces which produces sudden imprint formation and prominent pop-in responses is consistent with the pronounced strain bursts observed by Somekawa et al. for this orientation.

Experimental results are available in support of the dominant role played by twinning in the deformation of BCC metals subjected to extreme compressive stresses at the nanoscale [70]. Although the emergence of nanostructured regions and crystallites in BCC nanocontacts can be only hitherto supported *via* MD simulations, the sudden growth of the incepted substructure at the imprint's rim governs the prominent, recursive pop-in events found in (100) Ta surfaces along with the higher hardness value for this orientation. These responses coincide with the nanoindentation results for this orientation [15], which arguably supports the underlying defect mechanisms from our simulations.

In view of the possible role of strain rate effects, we have performed further massive MD simulations ($D = 100$ nm) of the first pop-in event at $v = 0.04$ m/s as well as under *static* conditions, where defect nucleation occurs under fixed indenter tip position over large simulation timeframes. The defect mechanisms in these simulations accurately reproduce those for $v = 0.2$ and 4 m/s.

4. Concluding remarks

1 Following the general contact mechanics relation in Eq. (3), our results indicate that the ratio between the contact pressure that yields defect nucleation, p_c, and the effective Young's modulus, E, provides a fundamental measure to the contact resistance as a function of the underlying defect nucleation mechanisms, surface orientation, and temperature. While the p_c of FCC Ni thus approaches that of BCC surfaces due to its high E, the p_c/E ratio in a given orientation remains constant in all FCC metals due to the onset of the same defect nucleation phenomenology. It is found that twin nucleation in (100) BCC surfaces occurs at a higher value of p_c/E than that associated with the partial dislocation nucleation events in FCC metals. The (111) surfaces of FCC metals are however intrinsically harder than the (110) surfaces of BCC metals. The variability of the p_c/E ratio with surface orientation and crystal structure underlies the clear role of the distribution of slip and twining systems beneath the surface upon defect nucleation, as well as the possible pressure sensitivity of the mechanisms. Defect inception in HCP Mg then generally occurs at smaller p_c *and* p_c/E than in the cubic metals. Our simulation results further assess the combined role of temperature and loading velocity on the defect nucleation processes, along with the influence of the applied indentation pressure upon the effective E. The currently found ≈25% increase in E at the onset of defect nucleation may then surpass the role of the elastic anisotropy on the load-penetration depth curves.

2 A transitional nanocontact regime occurs upon early defect inception. Under strict displacement-controlled tip penetration, this regime comprises recurrent quasi-elastic loading stages which lead to the onset of metastable contact configurations followed by secondary plastic instabilities or pop-ins, as evidenced by sudden load and hardness drops. The size of the instabilities is prescribed by the increase in the vertical displacement field $u(z)$ throughout the contact region, which results in load drop events, while the radial displacement field $u(r)$ is enhanced so as to promote pileup effects at the imprint's rim ($r = a$) along with an increase of the contact area. A steady-state is then instated characterized by the plateauing hardness p_p under self-similar defect network evolutions. The dislocation density at the plastic zone then reaches a constant ρ_p value irrespective of tip penetration. Since a more robust balance develops between the imprint formation mechanisms that limit the hardness p_p and the defect interlocking beneath the surface that hardens the material, the magnitude of the plastic instabilities is consequently reduced. In spite of the large indentation induced elastic strains, the well-developed imprint shape attained for steady-state indentations is not largely affected by the removal of the indenter tip from the surface. Our simulation results are supported by nanoindentation experiments in Cu, Al, Ni, Ta and Mg.

3 The extent of the transitional nanoindentation regime and the onset of steady-state responses is governed by the defect mechanisms occurring at the imprint and in the plastic zone. It is found that the secondary plastic instabilities are smaller in Cu and Ni than in Al surfaces due to the higher mobility of the less interlocked dislocation networks with smaller stacking fault ribbons in the latter. This leads to shorter transitional stages in FCC metals with large stacking width. The hardness p_p in Cu and Ni is limited by the nucleation of prominent lenticular twins throughout the imprint, which thus facilitate nanoimprint formation. This is counterbalanced by the strengthening provided within the heavily entangled defect networks at the plastic zone. While the p_p in Cu and Ni are then greater than in Al, this assertion is largely affected by the Young's modulus, as evidenced by the higher p_p/E of Al. A common imprint formation mechanism in FCC metals involves recurrent stacking fault interception, which produces zig-zagging slip traces that delineate the spherical shape of the indenter tip. Cross-slip processes of the surfaced screw dislocation segments in small stacking fault width Al are also detected.

4 Nanoimprint formation in BCC and HCP metal surfaces is characterized by recurrent twinning processes which produce nanostructured subgrain arrangements and crystallites. These mechanisms result in the larger secondary load drops and extended transitional regimes observed in (100) BCC Ta nanoimprints. As in the case of the lenticular nanotwins observed in large stacking fault width FCC metals, the growth of individual crystallites in BCC metals is promoted at the contact periphery where the maximum shear strain levels occur. Dislocation loop nucleation events from preexisting twins along with the cross-kinking of the surfaced screw dislocation segments are found to further contribute to imprint formation in BCC metals. In HCP Mg, the onset of nanostructured regions at the imprint is accompanied by the expansion of basal dislocation loops beneath the surface. The restricted interaction of the basal loops however suppresses the development of the archetypal, entangled dislocation networks observed in the cubic metals. Steady-state, self-similar indentations are then reached as the growth of the nanostructured regions scales with tip penetration while the basal dislocation loops continuously expand beneath the surface. While the p_p/E in HCP Mg is similar or even surpasses that of FCC Cu, the p_p/E is higher in the BCC surfaces. More pronounced thermal effects are also observed in the latter due to the enhancement of crystallite growth, which reduces the p_p/E.

5 An attempt to correlate nanocontact plasticity with the uniaxial response of the indented material beneath the surface is made through the p_p/σ_{ys} ratio. Since similar steady-state indentation responses and plastic zones are reached regardless of the preex-

isting defects at the indented surface, this ratio arguably represents a fundamental material parameter. In the current nanoindentation simulations, the p_p/σ_{ys} ratio ranges from ≈ 7 to ≈ 10 in FCC and BCC metals, respectively, largely exceeding the continuum plasticity *upper bound* prediction of ≈ 2.8. It is emphasized that while the strain gradients become sufficiently large so as to render invalid any continuity of the dislocation density throughout the minuscule material volume indented in our MD simulations, continuum plasticity accurately describes the yield stress under *uniaxial loadings* of the same material volume in the absence of the externally imposed strain gradients. Since a continuum plasticity framework that could be potentially applied to the analysis of low-load nanoindentations is thus lacking, the present correlation between nanoimprint formation and dislocation-mediated plastic yielding becomes particularly relevant. While the current nanoscale values of the p_p/σ_{ys} ratio concern the highest attainable hardness under the unique nanoimprint formation mechanisms reported in our investigation, this ratio gradually decreases toward the continuum mechanics bound of ≈ 2.8 when size-independent contact responses become at issue for larger micrometer-sized tip penetrations. Imprint formation and the expansion of the plastic zone then become in full compliance with the same basic continuum plasticity descriptions of dislocation glide and interaction [16,53].

Declaration of Competing Interest

The authors declare that they have no known competing financial interests or personal relationships that could have appeared to influence the work reported in this paper.

Acknowledgements

J.A. acknowledges financial support by Ministerio de Economía y Competitividad (Grants MAT2015-71347-P and PID2019-106744GB-I00 to the UPC). The work by J.O. and J.V. was sponsored by The Ministry of Education, Youth and Sports under grant CEDAMNF CZ.02.1.01/0.0/0.0/15_003/0000358 (Czech Republic). The work of J.V. was further supported by the Centre of Excellence for Nonlinear Dynamic Behaviour of Advanced Materials in Engineering, No. CZ.02.1.01/0.0/0.0/15_003/0000493, in the framework of the Operational Programme for Research, Development, and Education with institutional support RVO:61388998 (Czech Republic).

Supplementary materials

Supplementary material associated with this article can be found, in the online version, at doi:10.1016/j.actamat.2021.117122.

References

[1] C.L. Kelchner, S. Plimpton, Dislocation nucleation and defect structure during surface indentation, Phys. Rev. B - Condens. Matter Mater. Phys. 58 (1998) 11085–11088.
[2] O. Rodríguez de la Fuente, M.A. González, J.M. Rojo, J.A. Zimmerman, J. de la Figuera, J.C. Hamilton, W.W. Pai, Dislocation Emission around Nanoindentations on a (001) fcc Metal Surface Studied by Scanning Tunneling Microscopy and Atomistic Simulations, Phys. Rev. Lett. 88 (2002) 4.
[3] K.J. Van Vliet, S. Yip, S. Suresh, J. Li, T. Zhu, S. Yip, K.J. Van Vliet, J. Li, Quantifying the early stages of plasticity through nanoscale experiments and simulations, Phys. Rev. B - Condens. Matter Mater. Phys. 67 (2003) 1–15.
[4] J. Alcalá, R. Dalmau, O. Franke, M. Biener, J. Biener, A. Hodge, Planar defect nucleation and annihilation mechanisms in nanocontact plasticity of metal surfaces, Phys. Rev. Lett. 109 (2012).
[5] T.P. Remington, C.J. Ruestes, E.M. Bringa, B.A. Remington, C.H. Lu, B. Kad, M.A. Meyers, Plastic deformation in nanoindentation of tantalum: A new mechanism for prismatic loop formation, Acta Mater 78 (2014) 378–393.
[6] V. Navarro, O.R. De La Fuente, A. Mascaraque, J.M. Rojo, Uncommon dislocation processes at the incipient plasticity of stepped gold surfaces, Phys. Rev. Lett. 100 (2008) 1–4.
[7] S. Lee, A. Vaid, J. Im, B. Kim, A. Prakash, J. Guénolé, D. Kiener, E. Bitzek, S.H. Oh, In-situ observation of the initiation of plasticity by nucleation of prismatic dislocation loops, Nat. Commun. 11 (2020) 1–11.
[8] J.R. Morris, H. Bei, G.M. Pharr, E.P. George, Size effects and stochastic behavior of nanoindentation pop in, Phys. Rev. Lett. 106 (2011) 1–4.
[9] M.A. Lodes, A. Hartmaier, M. Göken, K. Durst, Influence of dislocation density on the pop-in behavior and indentation size effect in CaF2 single crystals: Experiments and molecular dynamics simulations, Acta Mater 59 (2011) 4264–4273.
[10] A. Barnoush, Correlation between dislocation density and nanomechanical response during nanoindentation, Acta Mater 60 (2012) 1268–1277.
[11] M.R. Maughan, D.F. Bahr, Discontinuous Yield Behaviors Under Various Pre-Strain Conditions in Metals with Different Crystal Structures, Mater. Res. Lett. 4 (2016) 83–89.
[12] D.F. Bahr, D.E. Kramer, W.W. Gerberich, Non-linear deformation mechanisms during nanoindentation, Acta Mater 46 (1998) 3605–3617.
[13] C.A. Schuh, Nanoindentation studies of materials, Mater. Today. 9 (2006) 32–40.
[14] Y. Shibutani, T. Tsuru, A. Koyama, Nanoplastic deformation of nanoindentation: Crystallographic dependence of displacement bursts, Acta Mater 55 (2007) 1813–1822.
[15] O. Franke, J. Alcalá, R. Dalmau, Z.C. Duan, J. Biener, M.M.M. Biener, A.M.M. Hodge, Incipient plasticity of single-crystal tantalum as a function of temperature and orientation, Philos. Mag. 95 (2015) 1866–1877.
[16] J. Alcalá, O. Casals, J. Očenášek, Micromechanics of pyramidal indentation in fcc metals: Single crystal plasticity finite element analysis, J. Mech. Phys. Solids. 56 (2008) 3277–3303.
[17] N. Zaafarani, D. Raabe, F. Roters, S. Zaefferer, On the origin of deformation-induced rotation patterns below nanoindents, Acta Mater 56 (2008) 31–42.
[18] H.J. Chang, M. Fivel, D. Rodney, M. Verdier, Simulations multi-échelles de l'indentation de métaux CFC: De l'atome au milieu continu, Comptes Rendus Phys 11 (2010) 285–292.
[19] B. Selvarajou, J.H. Shin, T.K. Ha, I.S. Choi, S.P. Joshi, H.N. Han, Orientation-dependent indentation response of magnesium single crystals: Modeling and experiments, Acta Mater 81 (2014) 358–376.
[20] E. Renner, Y. Gaillard, F. Richard, F. Amiot, P. Delobelle, Sensitivity of the residual topography to single crystal plasticity parameters in Berkovich nanoindentation on FCC nickel, Int. J. Plast. 77 (2016) 118–140.
[21] S. Plimpton, Fast parallel algorithms for short-range molecular dynamics, J. Comput. Phys. 117 (1995) 1–19.
[22] Y. Mishin, D. Farkas, M.J. Mehl, D.A. Papaconstantopoulos, Interatomic potentials for monoatomic metals from experimental data and ab initio calculations, Phys. Rev. B. 59 (1999) 3393–3407.
[23] Y. Li, J.B. Adams, D.J. Siegel, X.Y. Liu, Embedded-atom-method tantalum potential developed by the force-matching method, Phys. Rev. B - Condens. Matter Mater. Phys. 67 (2003) 8.
[24] R. Ravelo, T.C. Germann, O. Guerrero, Q. An, B.L. Holian, Shock-induced plasticity in tantalum single crystals: Interatomic potentials and large-scale molecular-dynamics simulations, Phys. Rev. B - Condens. Matter Mater. Phys. 88 (2013) 1–17.
[25] M.I. Mendelev, S. Han, D.J. Srolovitz, G.J. Ackland, D.Y. Sun, M. Asta, Development of new interatomic potentials appropriate for crystalline and liquid iron, Philos. Mag. 83 (2003) 3977–3994.
[26] D.Y. Sun, M.I. Mendelev, C.A. Becker, K. Kudin, T. Haxhimali, M. Asta, J.J. Hoyt, A. Karma, D.J. Srolovitz, Crystal-melt interfacial free energies in hcp metals: A molecular dynamics study of Mg, Phys. Rev. B. 73 (2006) 024116.
[27] I.A. Alhafez, C.J. Ruestes, Y. Gao, H.M. Urbassek, Nanoindentation of hcp metals: A comparative simulation study of the evolution of dislocation networks, Nanotechnology 27 (2015) 45706.
[28] C.J. Ruestes, I.A. Alhafez, H.M. Urbassek, Atomistic studies of nanoindentation—A review of recent advances, Crystals 7 (2017) 1–15.
[29] J. Varillas, J. Očenášek, J. Torner, J. Alcalá, Unraveling deformation mechanisms around FCC and BCC nanocontacts through slip trace and pileup topography analyses, Acta Mater 125 (2017).
[30] M. Yaghoobi, G.Z. Voyiadjis, Effect of boundary conditions on the MD simulation of nanoindentation, Comput. Mater. Sci. 95 (2014) 626–636.
[31] A. Stukowski, Visualization and analysis of atomistic simulation data with OVITO-the Open Visualization Tool, Model. Simul. Mater. Sci. Eng. 18 (2010).
[32] A. Stukowski, K. Albe, Dislocation detection algorithm for atomistic simulations, Model. Simul. Mater. Sci. Eng. 18 (2010) 025016.
[33] C. Begau, J. Hua, A. Hartmaier, A novel approach to study dislocation density tensors and lattice rotation patterns in atomistic simulations, J. Mech. Phys. Solids. 60 (2012) 711–722.
[34] Y. Gao, C.J. Ruestes, D.R. Tramontina, H.M. Urbassek, Comparative simulation study of the structure of the plastic zone produced by nanoindentation, J. Mech. Phys. Solids. 75 (2015) 58–75.
[35] J.W. Kysar, Y.X. Gan, T.L. Morse, X. Chen, M.E. Jones, High strain gradient plasticity associated with wedge indentation into face-centered cubic single crystals: Geometrically necessary dislocation densities, J. Mech. Phys. Solids. 55 (2007) 1554–1573.
[36] K. Durst, B. Backes, M. Göken, Indentation size effect in metallic materials: Correcting for the size of the plastic zone, Scr. Mater. 52 (2005) 1093–1097.

[37] G.M. Pharr, E.G. Herbert, Y. Gao, The indentation size effect: A critical examination of experimental observations and mechanistic interpretations, Annu. Rev. Mater. Res. 40 (2010) 271–292.
[38] K.L. Johnson, Contact Mechanics, Cambridge University Press, 1985.
[39] W. bing Li, K. Li, K. qi Fan, D. xing Zhang, W. dong Wang, Temperature and Pressure Dependences of the Elastic Properties of Tantalum Single Crystals Under <100>Tensile Loading: A Molecular Dynamics Study, Nanoscale Res. Lett. 13 (2018) 118.
[40] B. Luan, M.O. Robbins, The breakdown of continuum models for mechanical contacts, Nature 435 (2005) 929–932.
[41] M.A. Tschopp, D.L. McDowell, Influence of single crystal orientation on homogeneous dislocation nucleation under uniaxial loading, J. Mech. Phys. Solids. 56 (2008) 1806–1830.
[42] A. Garg, A. Acharya, C.E. Maloney, A study of conditions for dislocation nucleation in coarser-than-atomistic scale models, J. Mech. Phys. Solids. 75 (2015) 76–92.
[43] A. Garg, C.E. Maloney, Universal scaling laws for homogeneous dislocation nucleation during nano-indentation, J. Mech. Phys. Solids. 95 (2016) 742–754.
[44] G. Ziegenhain, H.M. Urbassek, A. Hartmaier, Influence of crystal anisotropy on elastic deformation and onset of plasticity in nanoindentation: A simulational study, J. Appl. Phys., American Institute of Physics AIP, 2010.
[45] S. Jiao, W. Tu, P. Zhang, W. Zhang, L. Qin, Z. Sun, J. Chen, Atomistic insights into the prismatic dislocation loop on Al (1 0 0) during nanoindentation investigated by molecular dynamics, Comput. Mater. Sci. 143 (2018) 384–390.
[46] Q. Liu, L. Deng, X. Wang, Interactions between prismatic dislocation loop and coherent twin boundary under nanoindentation investigated by molecular dynamics, Mater. Sci. Eng. A. 676 (2016) 182–190.
[47] Y. Sato, S. Shinzato, T. Ohmura, S. Ogata, Atomistic prediction of the temperature- And loading-rate-dependent first pop-in load in nanoindentation, Int. J. Plast. 121 (2019) 280–292.
[48] J.K. Mason, A.C. Lund, C.A. Schuh, Determining the activation energy and volume for the onset of plasticity during nanoindentation, Phys. Rev. B - Condens. Matter Mater. Phys. 73 (2006) 054102.
[49] J. Alcalá, D. Esqué-De Los Ojos, Reassessing spherical indentation: Contact regimes and mechanical property extractions, Int. J. Solids Struct. 47 (2010) 2714–2732.
[50] J. Alcalá, D. Esqué-de los Ojos, Extending the contact regimes to single-crystal indentations, Comptes Rendus - Mec 339 (2011) 458–465.
[51] G.M. Pharr, E.G. Herbert, Y. Gao, The Indentation Size Effect: A Critical Examination of Experimental Observations and Mechanistic Interpretations, Annu. Rev. Mater. Res. 40 (2010) 271–292.
[52] Y.Y. Lim, M.M. Chaudhri, The influence of grain size on the indentation hardness of high-purity copper and aluminium, Philos. Mag. A Phys. Condens. Matter, Struct. Defects Mech. Prop. 82 (2002) 2071–2080.
[53] J. Alcalá, D. Esqué-De Los Ojos, J. Očenášek, Extracting uniaxial responses of single crystals from sharp and spherical hardness measurements, Mech. Mater. 84 (2015) 100–113.
[54] A. Hasnaoui, P.M. Derlet, H. Van Swygenhoven, Interaction between dislocations and grain boundaries under an indenter - A molecular dynamics simulation, Acta Mater 52 (2004) 2251–2258.
[55] C. Huang, X. Peng, T. Fu, X. Chen, H. Xiang, Q. Li, N. Hu, Molecular dynamics simulation of BCC Ta with coherent twin boundaries under nanoindentation, Mater. Sci. Eng. A. 700 (2017) 609–616.
[56] B.R. Kuhr, K.E. Aifantis, Interpreting the inverse Hall-Petch relationship and capturing segregation hardening by measuring the grain boundary yield stress through MD indentation, Mater. Sci. Eng. A. 745 (2019) 107–114.
[57] J. Alcalá, J. Očenášek, J. Varillas, J.A. El-Awady, J.M. Wheeler, J. Michler, Statistics of dislocation avalanches in FCC and BCC metals: dislocation mechanisms and mean swept distances across microsample sizes and temperatures, Sci. Rep. 10 (2020) 19024.
[58] I.J. Spary, A.J. Bushby, N.M. Jennett, On the indentation size effect in spherical indentation, Philos. Mag. 86 (2006) 5581–5593.
[59] S.K. Lawrence, D.F. Bahr, H.M. Zbib, Crystallographic orientation and indenter radius effects on the onset of plasticity during nanoindentation, J. Mater. Res. 27 (2012) 3058–3065.
[60] M.M. Biener, J. Biener, A.M. Hodge, A.V. Hamza, Dislocation nucleation in bcc Ta single crystals studied by nanoindentation, Phys. Rev. B - Condens. Matter Mater. Phys. 76 (2007) 1–6.
[61] H. Somekawa, T. Tsuru, A. Singh, S. Miura, C.A. Schuh, Effect of crystal orientation on incipient plasticity during nanoindentation of magnesium, Acta Mater 139 (2017) 21–29.
[62] D. Catoor, Y.F. Gao, J. Geng, M.J.N.V. Prasad, E.G. Herbert, K.S. Kumar, G.M. Pharr, E.P. George, Incipient plasticity and deformation mechanisms in single-crystal Mg during spherical nanoindentation, Acta Mater 61 (2013) 2953–2965.
[63] E. Carrasco, M.A. González, O. Rodríguez De La Fuente, J.M. Rojo, Analysis at atomic level of dislocation emission and motion around nanoindentations in gold, Surf. Sci. 572 (2004) 467–475.
[64] W. Xia, G. Dehm, S. Brinckmann, Insight into indentation-induced plastic flow in austenitic stainless steel, J. Mater. Sci. 55 (2020) 9095–9108.
[65] M. Rester, C. Motz, R. Pippan, Microstructural investigation of the volume beneath nanoindentations in copper, Acta Mater 55 (2007) 6427–6435.
[66] E. Demir, D. Raabe, N. Zaafarani, S. Zaefferer, Investigation of the indentation size effect through the measurement of the geometrically necessary dislocations beneath small indents of different depths using EBSD tomography, Acta Mater 57 (2009) 559–569.
[67] A.J. Cackett, C.D. Hardie, J.J.H. Lim, E. Tarleton, Spherical indentation of copper: Crystal plasticity vs experiment, Materialia 7 (2019) 100368.
[68] S. Wang, S. Liu, D. Zhao, Z. Wang, H. Zhao, Indentation on monocrystalline copper at cryogenic and ambient temperature, Materialia 9 (2020) 100510.
[69] C. Zambaldi, C. Zehnder, D. Raabe, Orientation dependent deformation by slip and twinning in magnesium during single crystal indentation, Acta Mater 91 (2015) 267–288.
[70] J. Wang, Z. Zeng, C.R. Weinberger, Z. Zhang, T. Zhu, S.X. Mao, In situ atomic-scale observation of twinning-dominated deformation in nanoscale body-centred cubic tungsten, Nat. Mater. 14 (2015) 594–600.
[71] P.M. Larsen, S. Schmidt, J. Schiøtz, Robust structural identification via polyhedral template matching, Modelling Simul. Mater. Sci. Eng. 24 (2016) 055007.